TECHNICAL REPORT

SPACE TELESCOPE SCIENCE INSTITUTE
Operated for NASA by AURA

Title: Simulations of MIRI Four-Quadrant Phase Mask Coronagraph (III): Target Acquisition and CCC Mechanism Usage	Doc #: JWST-STScI-003546, SM-12 Date: 29 October 2013 Rev: -
Authors: C-P. Lajoie, D. Hines, R. Soummer and The Coronagraphs Working Group Phone: 410 – 338 - 5007	Release Date: 6 March 2014

1 Abstract

We present the results of simulations of target acquisition with the four-quadrant phase masks (4QPM) on the Mid-Infrared Instrument (MIRI). We approach the problem from an operational point of view and (1) evaluate the effect of latency due to the acquisition of successive images without using the contamination control cover (CCC) and (2) derive raw contrast curves for all three 4QPM coronagraphs. Using a 1% latency that decays exponentially over a folding time of 300 seconds, as well as photon, background, and detector noise sources, our results show that latency can be mitigated and the use of CCC limited. In particular, our simulations suggest that the raw contrast varies between the three 4QPM, with the best raw contrast achieved at 10.65 μm and decreasing by an order of magnitude at 15.50 μm. The main limiting factor on contrast at longer wavelengths is the contribution from the background, at least for the magnitudes used here, whereas, on the other hand, the slew accuracy model affects contrast to a lesser degree. We find no evidence of latency contamination or residuals after 10,000 seconds in the raw contrast curves and simulated coronagraphic images derived here, assuming our simple model for latency. In general, our simulations suggest that a raw contrast of ~$10^{-5.5}$-$10^{-4.5}$ can be reached in a few thousands of seconds, although background photon noise might put tighter limits on these values. Based on our results, we recommend not using the CCC during target acquisition operations to relieve operational constraints on the overall CCC mechanism usage and MIRI thermal budgets. This work will also tie in the implementation of coronagraphy in the future JWST Exposure Time Calculator (ETC). Based on our simulations, we find that the CCC is not required for stars of magnitude up to 0.

2 Introduction

The contamination control cover (CCC) on MIRI is a cover at the entrance aperture of MIRI designed to block any light from entering it and protect the hardware, such as the detectors. The MIRI Operations Concept document (OCD) Version C currently specifies

that during routine observations the CCC will be used during acquisition of dark images for the MRS and during Target Acquisition of bright objects for coronagraphy to avoid strong latent images. Based on estimates of mechanism usages based on likely observing scenarios from the SODRM 2012, the number of CCC moves (open and close cycles) will vastly exceed the mechanism qualification over the expected lifetime of the mission (Hines et al. 2014). Moreover, the thermal load of one CCC cycle, which is equivalent to 17 filter wheel moves, imposes strong limitations on the rate of use of the mechanism (Hines et al. 2014). As discussed in detail in Lajoie et al. 2012, in addition to multiple CCC cycles, target acquisition for the MIRI 4QPM requires multiple slews (e.g. Twin or Quad TA scenarios) and the use of the neutral density filter (FND). In order to reach, for example, the F1550C coronagraphic filter after TA using the neutral density filter, five filter moves are necessary (see Figure 1). Therefore, the combined use of the filter wheel and the CCC adds thermal load to the system and adds overhead for the mechanism moves. It is therefore imperative to assess whether the CCC is vital for operations of MIRI and whether latency can be mitigated.

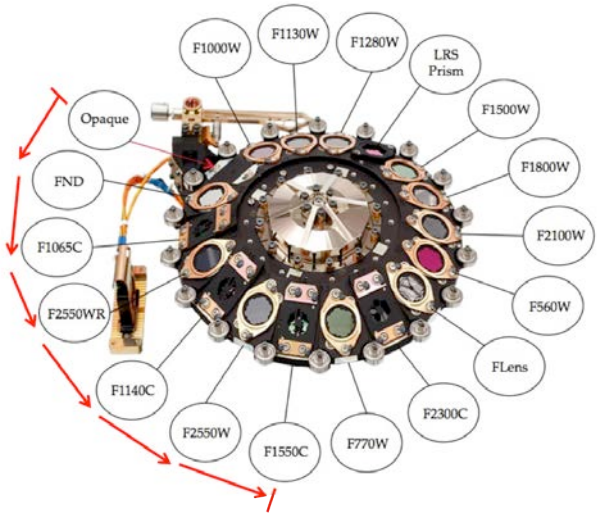

Figure 1: MIRI filter wheel showing the various filters in between the FND used for target acquisition and the furthest coronagraphic filter F1550C.

3 Computational Method

We assume that target acquisition (TA) was already performed with the FND filter, that the star is as close to the 4QPM center as possible, and that we are ready to rotate the filter wheel to the requested coronagraphic filter without using the CCC. Residual images from intermediate filters can be imprinted onto the detector as the filter wheel rotates to reach the desired coronagraphic filter; we estimate that the worst-case scenario for coronagraphy occurs when going from the FND to the furthest coronagraphic filter (F1550C). We simulate the rotation of the filter wheel by stacking subsequent latent images in time until integration on the F1550C filter has started. For completeness, we also perform similar simulations for the F1065C and F1140C 4QPM. We describe this image manipulation below.

3.1 Construction of coronagraphic images

Our approach for simulating latency is based on the simple manipulation of coronagraphic images. We create our coronagraphic images using the same code as described in Soummer & Makidon (2010) and, more recently, Lajoie et al. 2012. This code propagates the electric field from the pupil plane to the focal plane using successive Fast Fourier Transforms (FFTs). We use a starting wavefront error map (Rev. V) and incorporate the different intervening masks, filters, and Lyot stops, as well as realistic transmission profiles for the filters and the 4QPM's Germanium coating. The resulting image pixels are then matched to the MIRI pixel size. By construction, our images are normalized to 1 photon and therefore need to be scaled to the right number of photons depending on the spectral type of the target and its distance. Here, we use a Vega-like blackbody of 9,600 K with a radius of 2.36 $R_{\odot}$ and a distance of 7.68 pc, which we multiply by the respective filter's bandpass, Germanium transmission, and detector quantum efficiency (see Figure 2).

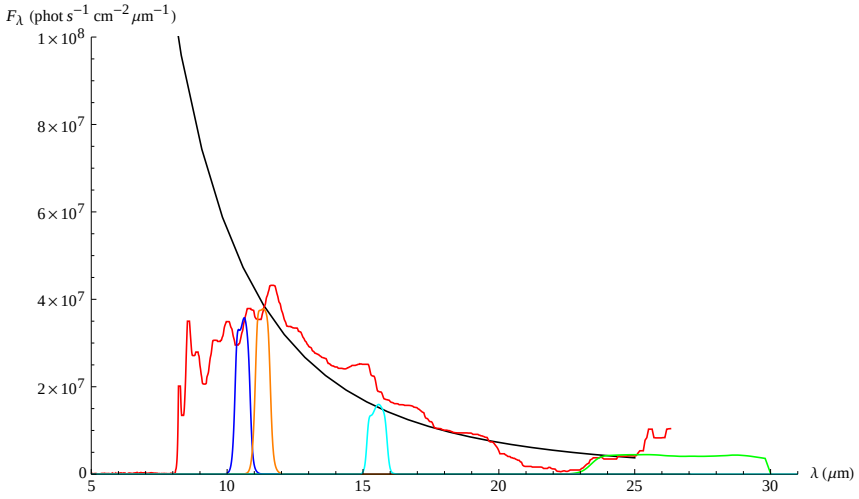

Figure 1: Blackbody (9,600 K, 2.36 $R_{\odot}$, 7.68 pc) used for the simulated images along with the various filter's bandpass scaled used: F1065C (blue), F1140C (orange), F1550C (cyan), F2550W (green), and FND (red). The germanium and detector quantum efficiency are not included here.

Note that the Optical Telescope Element (OTE) and MIRI throughputs are not included in our simulations. We estimate their effect to a loss of about 1 magnitude, which means a star of magnitude 5 in our simulations would really be a magnitude 4 before entering the OTE and MIRI due to throughput losses. We estimate the effects of the OTE throughputs on our conclusions to be minor only and do not foresee more simulations including OTE/MIRI throughputs. For example, for the F1065C and FND filters, we get 2.5×10^8 phot sec^{-1} and 4.5×10^6 phot sec^{-1} respectively. Our starting images for the 4QPM at 15.50 um are shown in Figure 3 and are simply scaled up or down depending on exposure time and decay time.

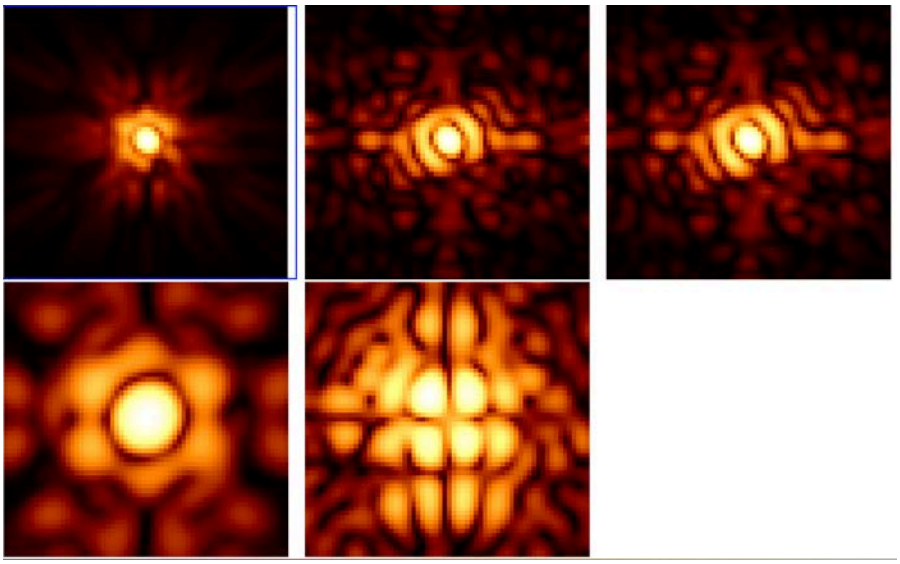

Figure 2: Point spread functions centered on the 4QPM 1550 for the filters used in this study. Clockwise, starting top left: FND, F1065C, F1140C, F2550W, and F1550C. Note that the images are not plotted on the same intensity scale. See also Figures 4 and 5.

3.2 Light leak during filter wheel rotation

The effect of rotating the filter wheel while light is falling onto the detector is investigated here. As we will show, rotation of the coronagraphic filter, to which the Lyot stops are attached, changes the amount of diffracted light that is actually "stopped" by the Lyot Stop and therefore leads to light leaks.

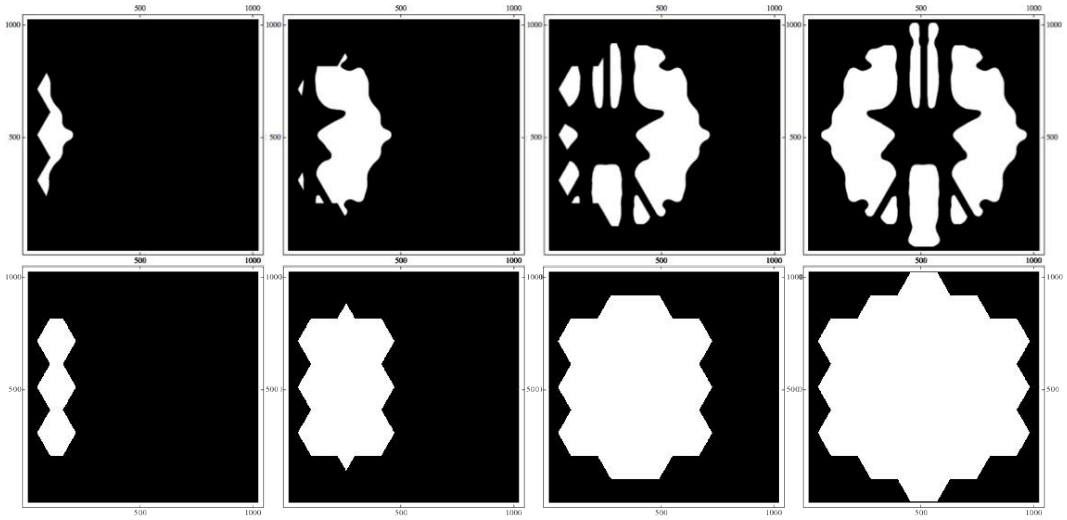

Figure 4: Filter wheel rotation for the coronagraphic filters (top row) and other filters (bottom row). From left to right: 25%, 50%, 75%, and 100% aligned. PSFs are generated for the full passage of the filter from one side to the other in the same increments as shown here. See also Figures 3 and 5.

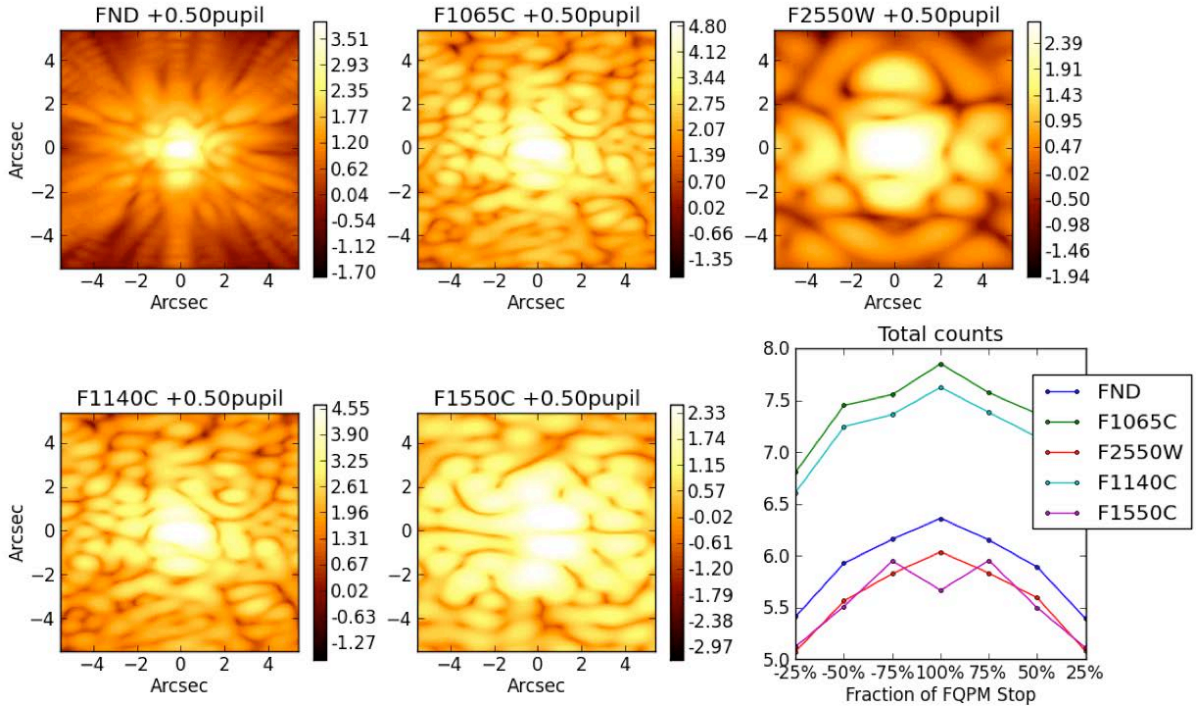

Figure 3: FQPM1550 PSF for different filters and 50% filter wheel alignments (see Figure 4). The bottom right panel shows the total counts in each image as a function of filter wheel alignment. For the combination FQPM1550 and F1550C, a temporary misalignment of the filter wheel with the pupil lead to more counts leaking to the detector because the FQPM rejects the starlight outside of the geometric pupil in the Lyot plane. See also Figures 3 and 4.

The main consequences of varying the pupil size are: (1) increased PSF size, therefore spreading light where there would not be otherwise; and (2) possible increased intensity of light given that the coronagraphic stops are not aligned and that diffracted light may leak in. Figure 4 shows the stops used for the different filters as they are rotated to their nominal position. The cold stop on the left is used for the FND and F2550W filters, and the FQPM stop on the right is used for the three coronagraphic filters, namely F1065C, F1140C, and F1550C. Figure 5 shows PSFs for all the filters considered here for the case where the stops are halfway in position (just like in Figure 4). The configuration is FQPM1550 + filter + corresponding stop. As expected, the smaller effective pupil increases the size of the PSF in the direction of rotation. The bottom right panel of Figure 5 also shows the total counts in each filter image as a function of the fraction of the stop. For all filters except F1550C, a smaller pupil leads to fewer counts, which is expected.

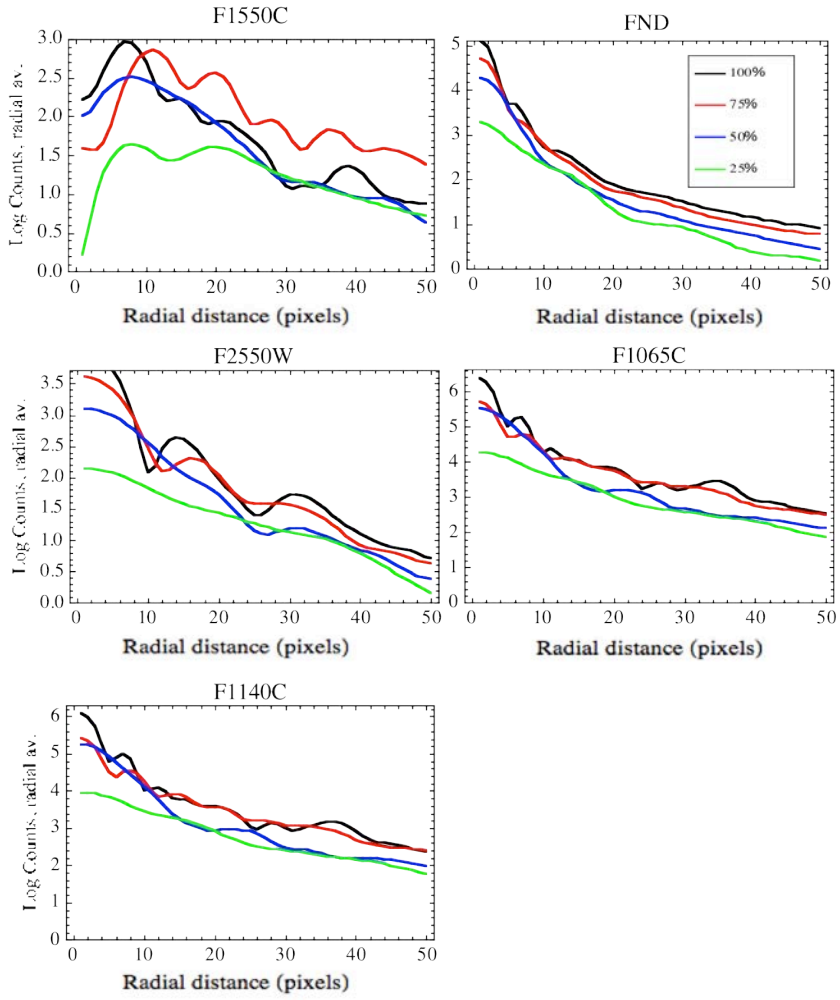

Figure 6: Azimuthal average of PSF for FQPM1550 for different filters and different filter wheel alignments (100%, 75%, 50%, and 25% aligned). Only for the corresponding coronagraphic filter (see F1550C with FQPM1550 above) does a partial pupil (e.g. 75%) introduce more light and spreading of the PSF. See text.

For F1550C however, since the 4QPM diffracts light to specific regions of the Lyot plane pupil, a slight offset of the FQPM stop leads to a sharp increase in light leaking through. In fact, Figure 5 shows that there are as many counts at 25% pupil-size as when the stop is aligned. This is shown also in Figure 6, where we show azimuthal averages for the various filters used and different fractions of the stop. Although the PSF are not symmetrical anymore because of the clipped pupil, we see that the effect of the cold/FQPM stop rotation is to spread the light out to larger separations. Also, the intensity of the leaking light also decreases as the cold/FQPM stop is moved out, except for F1550C. Indeed, in the case of F1550C, a shift of the FQPM stop lets the diffracted light in the detector and the effectiveness of the coronagraph is substantially decreased.

Based on the results of Figures 5 to 7, we decided to include images during transitions from one filter to another. We modeled images for each filter using 25%, 50%, 75%, and 100%, simulating the motion of the stop from one side to the other. In all, we have seven images per filter. Based on the MIRI OBA design description document (Renouf et al. 2011), we also allow 25 seconds to go from one filter to the next one, yielding an average

of ~3 seconds per intermediate positions used here. When the filter is in position, it stops for a dwell time of 8 seconds (Renouf et al. 2011).

3.3 Implementation of latency

Following the findings of Greene & Walker (2013; other private communication from G. Rieke), which is based on flight model testing, the residual image intensity is about 1% of the source and decays exponentially with a folding time of 300 seconds. Note that Greene & Walker 2013 identify various timescales for the decay of latents and that longer ones may exist. We investigate the effect of longer timescales in §4. Interestingly, the numbers reported by Greene & Walker (2013) apply to both saturated and unsaturated data (point and extended sources). We apply this latency factor to every pixel of our images *after every detector reset* which, in coronagraphy, is 0.242 seconds, and propagate the resulting (decaying) image in time. Although there is a dwell time of 8 seconds for every filter wheel move, the detector is constantly reset (sub-array frame time is 0.242 seconds) during the transition from the neutral density filter to the coronagraphic filter of interest. No image is therefore integrated for more than a frame time. We note that detector effects such as saturation and non-linearity are not modeled.

3.4 Noise sources

We include noise sources such as photon, detector, and background photon noise in our simulations. Detector noise is characterized by a readout noise of 10 electrons and a pixel-to-pixel variation of 3%. The background photon noise is estimated from Figure 4, where the total number of photons is summed up over one pixel (0.11×0.11 arcsec^2) and integrated over each filter bandpass as well as the 4QPM germanium transmission profile and the detector quantum efficiency. In this manner, for example, we get ~22 electrons per pixel per second for both the F1065C and F1140C filters, whereas the F2550W filter allows ~155 electrons per pixel per second. Table 1 summarizes the background noise values used for each filter.

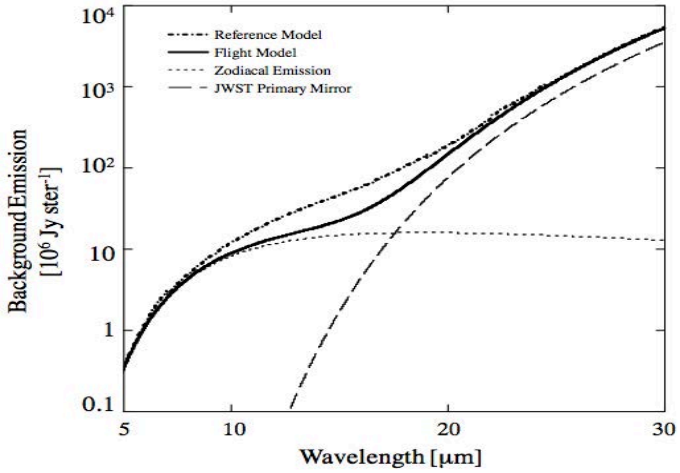

Figure 7: MIRI background components from which we estimate the number of photons per second in each filter bandpass. Taken from Glasse (2010).

Table 1 Background noise for each filter used in this analysis.

FILTER	BACKGROUND (photons/second/pixel)
FND	1
F1065C	22
F1140C	24
F1550C	12
F2550W	155

4 Simulation Results

We now assess the raw contrast performance of all three coronagraphic masks and filters by using multiple combinations of target and reference positions to derive contrast curves. First, using an accuracy model (e.g. CDR or REQ; see Figure 8), we generate ~50 different random pointings using the Single TA scenario, for each of which we generate a set of PSF images (including images for intermediate filter wheel alignment; see section 3.2).

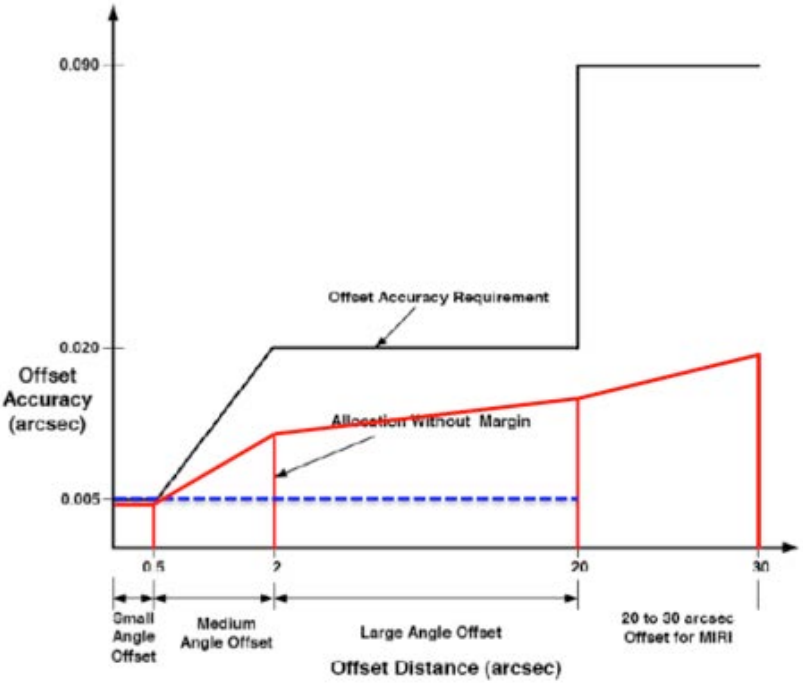

Figure 8: Slew accuracy models. Requirement slew accuracy (black) and 'ACS-software CDR' slew accuracy (blue). The Expected model (red) is not used in this paper.

From these ~50 random pointings, we make all possible combinations (~1200) to simulate the positions of both the target and the reference stars and generate a contrast image for each of them. We define the raw contrast as the azimuthal average of the contrast image normalized by the peak of an off-axis PSF. Our definition of raw contrast therefore does not constitute a detection limit but is rather only a useful metric to assess the performances of the 4QPM.

An example of our procedure for deriving contrast for F1550C is shown in Figure 9 for only one combination of target and reference positions. The target and reference are

assumed to be of the same spectral type but different magnitudes. The images are scaled up according to exposure time, but since we try to match the signal levels between the target and the reference, the different magnitudes result in different exposure times, noise levels, and latency contamination. Here, we use a reference star 2 magnitudes brighter than the target star and we perform a simple PSF subtraction (shown in lower left panel Figure 8). These residuals are then normalized by the maximum pixel value of the "pure" target image taken without the 4QPM coronagraph (top right panel), and the result is a raw contrast image. The lower right panel of Figure 8 shows the average and maximum contrast (blue and red curves respectively) as a function of time *with no noise sources, no offset from the center of the 4QPM, and no offset between the target and the reference*. In this particular case, the contrast curve shows that the longer the target image is integrated, the larger the achieved contrast gets. Also, in this case, only the different latents between the target and the reference actually limit how far down the contrast curve can reach. We also point out that, as a validation check, we also ensured that the normalized residuals for integrations with no noise and no latents are indeed zero.

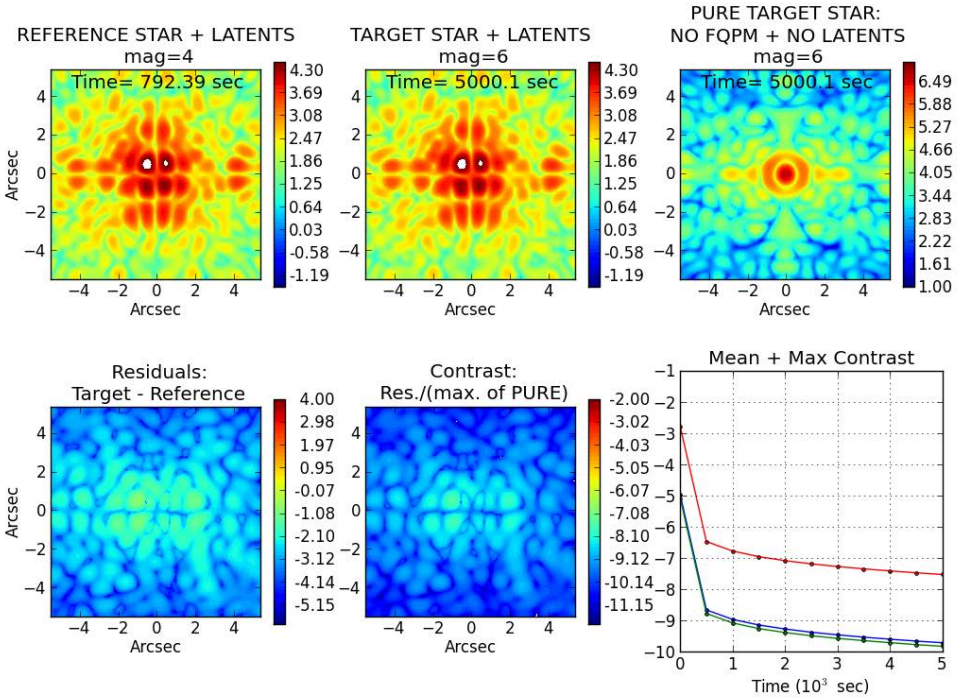

Figure 9: Procedure for deriving raw contrast from one pair of target and reference image set. Latents are included. Left to right, from top row: Reference image, Target Image, Non-coronagraphic Target image, Residual (simple PSF subtraction), Raw contrast image, and average/maximum contrast as a function of time.

4.1 Raw Contrast and Exposure Time

Figure 10 shows similar contrast curves as a function of exposure time for scenarios including offset between target and reference stars as well as all the noise sources and latent images. In all cases, the first hundreds of seconds are the most important as the average and maximum contrasts improve very steeply. After ~500-1000 seconds, the contrast reaches a slow linear regime until the end of the simulation. We note however

that an offset between the target and the reference or the addition of noise (at least at 15.50µm, as is shown if Figure 10) quickly dominates over the effect of latency and the contrast curves level off at around 10^{-6}-10^{-5}. It is important to note at this point that our results apply for the particular spectrum used here, namely a Vega-like blackbody. For fainter stars or redder objects, the relative contributions from the target, latents, and backgrounds will differ and might impact the contrast performances in different proportions.

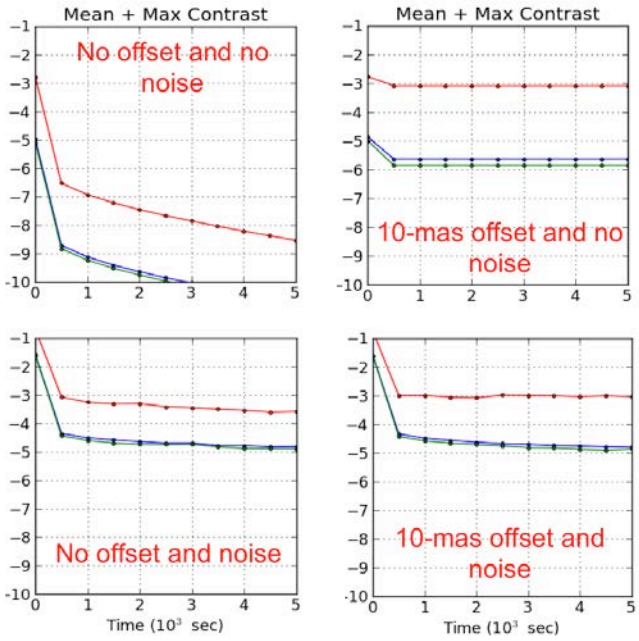

Figure 10: Average contrast (blue), maximum contrast (red), and contrast at 10 λ/D on a logarithmic scale as a function of exposure time for FQPM1550 and different scenarios. *Top left*: Perfect pointing and no noise; *Bottom left*: Perfect pointing and noise; *Top right*: Offset between target and reference and no noise; *Bottom right*: Offset between the target and the reference and noise. Here, "noise" implies all noise sources.

4.2 Raw Contrast Performance: Azimuthal Averages

From our ~1200 different contrast images combining all possible pointing pairs for the target and reference, we can also derive average azimuthal contrast curves, as shown in Figures 11 and 12 (for the CDR and REQ slew accuracy models respectively). The average azimuthal curves as well as the +/- 1σ levels are computed at every radial distance bin for each contrast image. Each panel of Figures 10 and 11 shows the contrast performance of the 4QPM at 10.65, 11.40, 15.50 µm for integration times of 10,000 seconds, whereas the insets show the random pointings errors from the TA process both for the target and reference stars using the Single TA scenario.

Overall, we observe that the contrast at 10 λ/D*[1] is around $10^{-5.5}$ for the 10.65 µm and 11.40 µm 4QPM, and decreases to ~$10^{-4.5}$ at 15.50 µm. We observe this decrease in contrast as a function of wavelength for both the CDR and REQ slew accuracy models

*[1] The contrast at 10 λ/D corresponds to the updated metric for the MIRI coronagraph contrast requirements

and we attribute its cause to the sharp decrease in flux from the star with wavelength mixed with the relatively larger contribution of the background noise at longer wavelengths (see Figure 6).

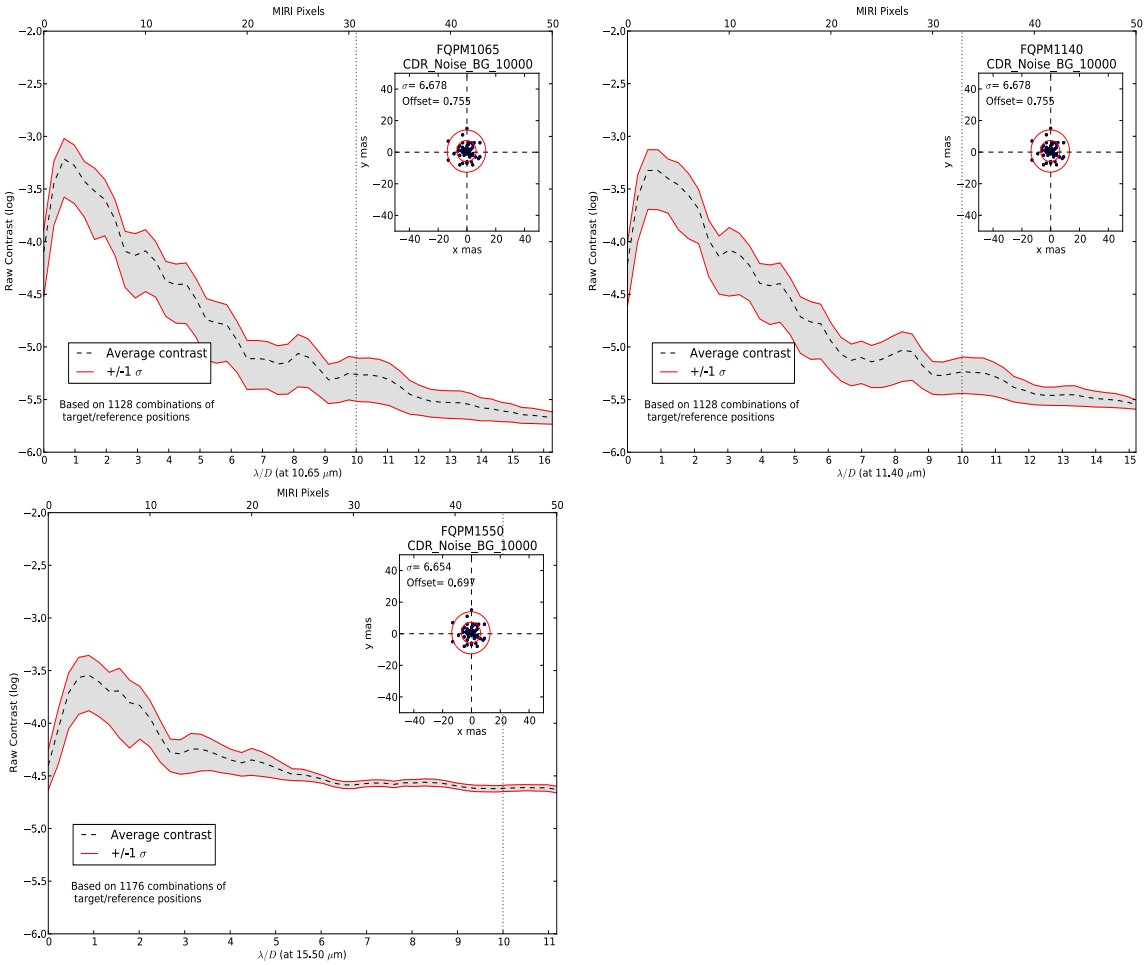

Figure 11: Contrast performances for the 10.65, 11.40, and 15.50 µm 4QPM (top, middle, bottom respectively) for the CDR slew accuracy model including noise at 10,000 seconds. The dashed line shows the average of ~1200 contrast curves whereas the red lines show the +/- 1 sigma standard deviation. The top X-axis shows the size of MIRI pixels, whereas bottom X-axis shows the corresponding scale in λ/D. The insets show the random pointings generated with the CDR slew accuracy model using the Single TA scenario. In this particular simulation (Vega-type spectrum, magnitude 6) the background limitation is particularly obvious at 15.5 micron.

Figures 11 and 12 also show that the peak of the average contrast curve goes down with wavelength, opposite to what is observed at 10 λ/D. We attribute this peak of larger contrast at longer wavelengths to the fact that the PSF is also larger in size (scales as λ/D). Indeed, small offsets between the target and the reference are smoothed out by the larger PSF size at 15.50 µm and the subtraction of the two offset PSFs is better. Figure 13 shows a cartoon of offset PSFs and their respective subtraction.

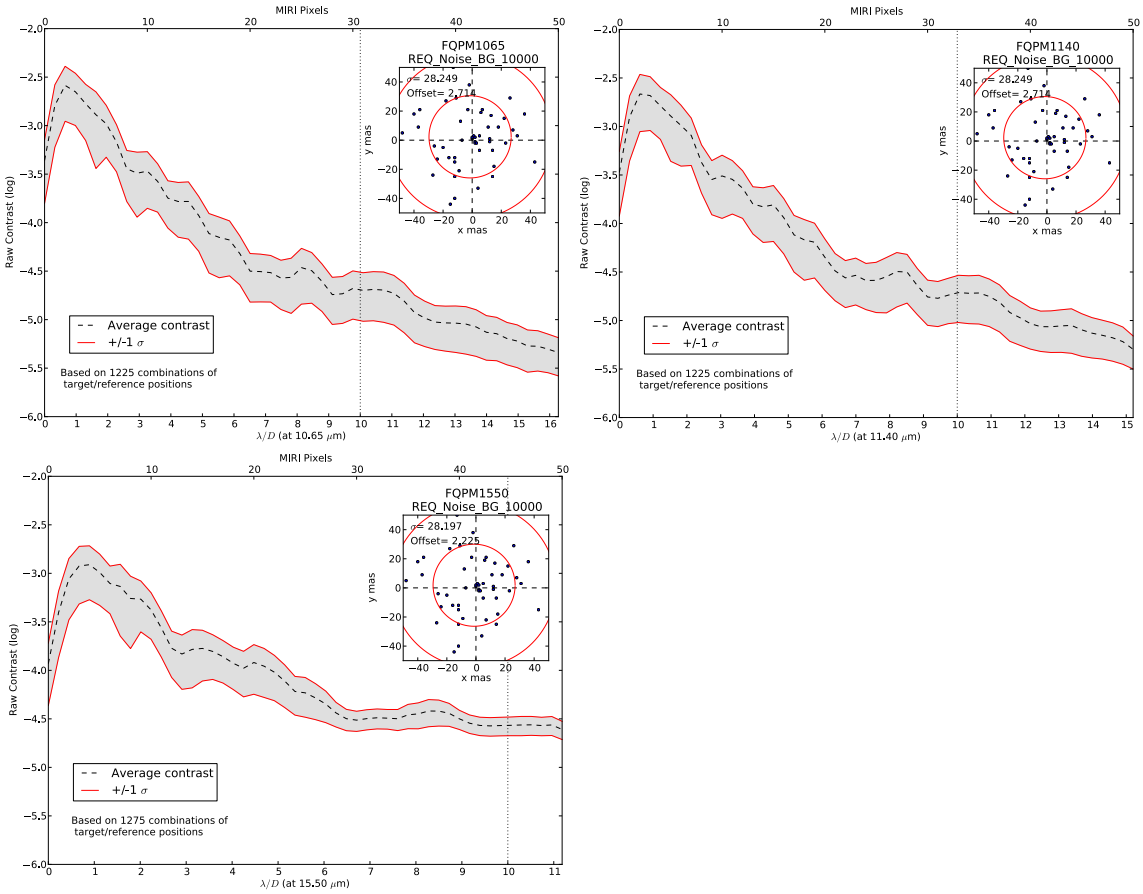

Figure 4: Contrast performances for the 10.65, 11.40, and 15.50 µm 4QPM (top, middle, bottom respectively) for the REQ slew accuracy model including noise at 10,000 seconds. The dashed line shows the average of ~1200 contrast curves whereas the red lines show the +/- 1 sigma standard deviation. The top X-axis shows the size of MIRI pixels, whereas bottom X-axis shows the corresponding scale in λ/D. The insets show the random pointings generated with the REQ slew accuracy model using the Single TA scenario.

An obvious difference between CDR and REQ models however is seen at the peak of the contrast curves, where a 0.5 decimal exponent improvement is observed for the CDR slew accuracy model. For the 4QPM at 10.65 and 11.40 µm, the improvement due to the pointing accuracy is of the same order of magnitude beyond 10 λ/D. However, at 15.50 µm, the effect of pointing accuracy is dominated by the contribution of the background noise and no difference is observed between the CDR and REQ slew accuracy models beyond ~6 λ/D. The effect of pointing accuracy (REQ vs CDR) is also apparent when looking at the standard deviations of the contrast curves at large λ/D.

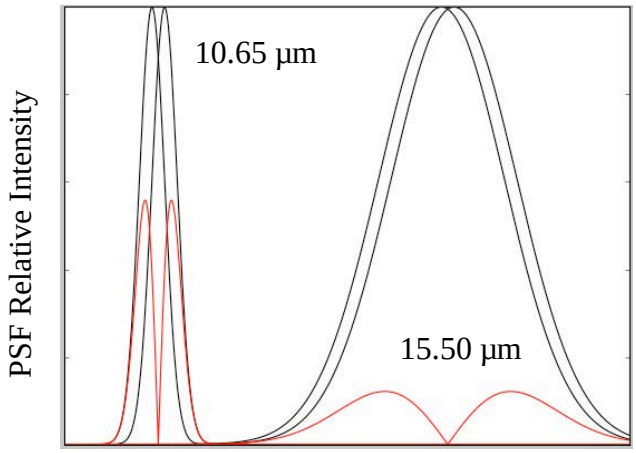

Figure 13: Cartoon showing the effect of a small offset of PSFs at different wavelengths (black lines) and their simple subtraction (red lines), mimicking an offset between a target and a reference stars. Two larger PSF (e.g. 15.50 um) smooth out the small offset and the subtraction is better than at shorter wavelengths.

Figure 14, on the other hand, shows the effect of adding noise on contrast performance for the 4QPM at 10.65 µm (top row) and 15.50 µm (bottom row). Panels on the left show the contrast curves with no noise whereas panels on the right have all noise sources. It is obvious that the background noise at 10.65 µm (also for 11.40 µm, although not shown here) does not affect the contrast performance of the coronagraph, unlike the 4QPM at 15.50 µm where the addition on noise decreases contrast by ~0.5 dex. Also, as expected, longer exposure times lead to improving contrast *at large λ/D*. The results presented here are all derived at 10,000 seconds exposure time and should be considered as upper limits; shorter exposure times will necessarily lead to more limited contrast performance.

Overall, our results show that contrast performances for the 4QPM at 15.50 µm are mostly limited by the background noise and to a lesser extent, by the pointing accuracy. For the coronagraphs at shorter wavelength, the slew accuracy model mainly determines the shape and level of the contrast curves with little to no contribution from the background. We emphasize that these conclusions should hold true for target and reference stars of magnitudes 6 and 4 respectively, or brighter; dimmer stars will be impacted to a larger degree at all wavelengths by the background photon noise.

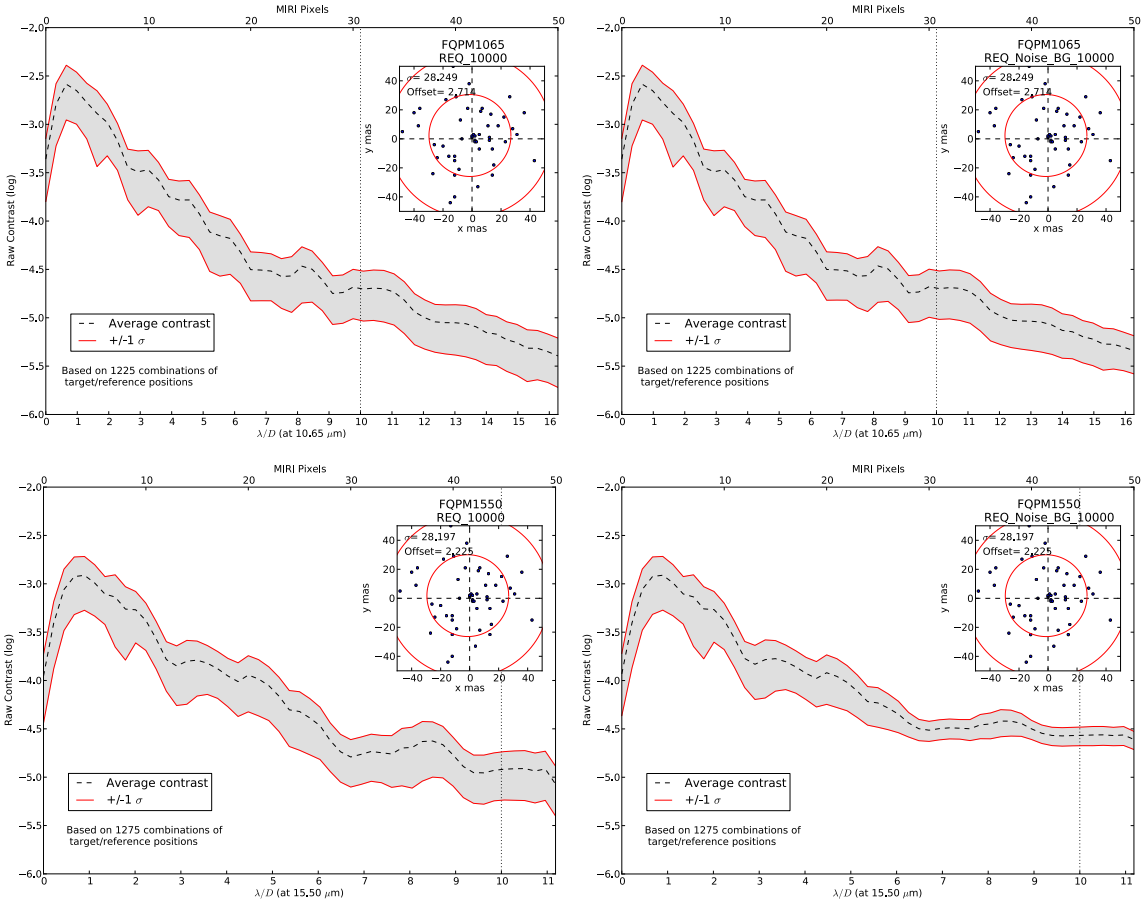

Figure 14: Comparison of contrast curve without any noise (left panels) and with all noise sources (right panels), both with the REQ slew accuracy model. Top row is for 4QPM 1065 and bottom row is for 4QPM 1550. The effect of background noise is only noticeable at longer wavelengths, at least for the magnitudes selected in this study.

Finally, we show in Figure 15 contrast curves for the 4QPM 1140 coronagraph for different target and reference magnitudes. Vega magnitudes for target and reference are, respectively, -1 and 3 (top left), 6 and 4 (top right), and 10 and 8 (bottom). The effect of using dimmer target stars is obvious: the background photon noise increasingly dominates and limits the contrast performance. Indeed, for the brightest case (top left panel), the contrast is even larger than for dimmer stars because the relative contribution of the background photon noise is much smaller, thus improving contrast. Given our latency prescription, our results suggest that latents can be mitigated without resorting to using the CCC mechanism for stars as bright as magnitude 0.

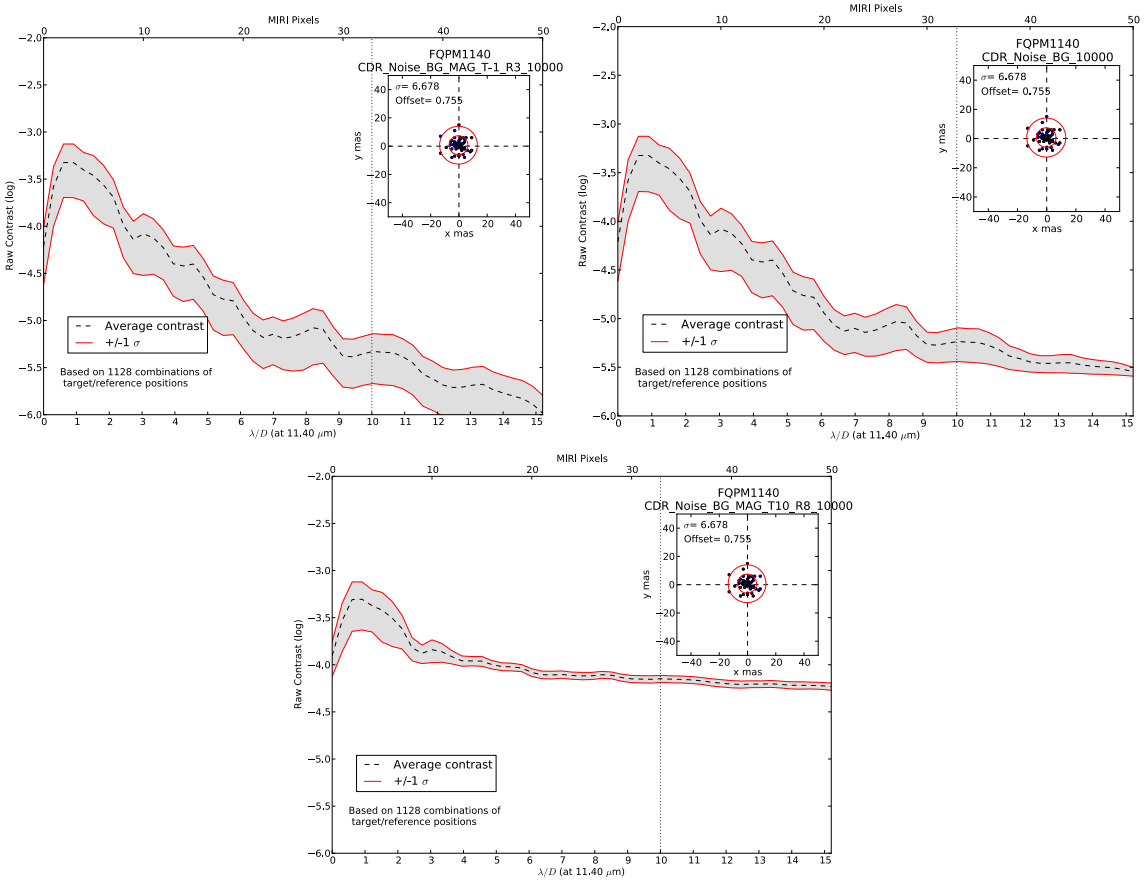

Figure 15: Effect of changing the magnitudes of the target and reference on contrast performances for the 4QPM at 11.40 µm. Magnitudes for target and reference are, respectively, -1 and 3 (top left), 6 and 4 (top right), and 10 and 8 (bottom).

4.3 Latency prescription

Given the relative uncertainty on the latency characterization (~30%; Greene & Walker 2013), we explore a few different scenarios involving larger initial values and longer folding times. Although a definitive prescription for the MIRI detector is not yet available, it can be argued that harder saturation levels produce longer lasting charge trapping and persistent images. On the other hand, shorter timescales would be beneficial here since latents would fade away faster. It is important to note at this point that we do not model detector saturation effects and that there exists the possibility of multiple latency decay timescales, which we do not model either.

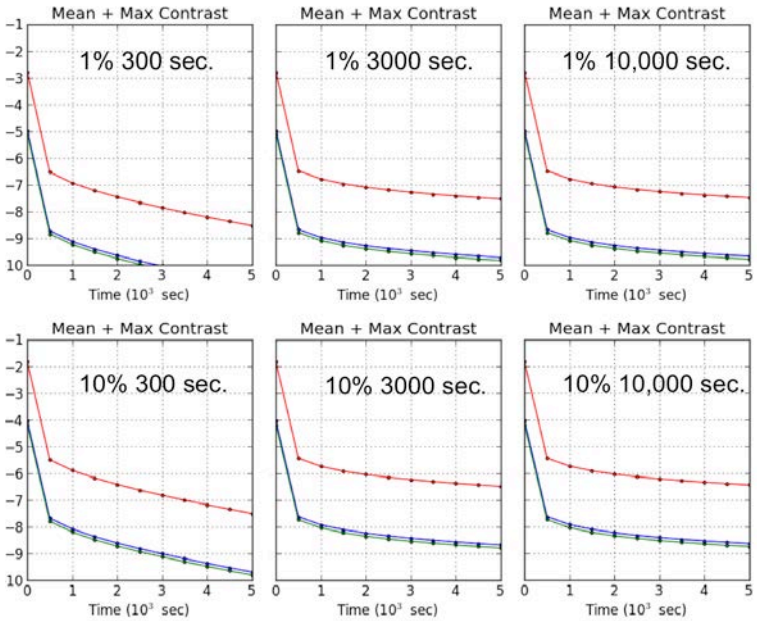

Figure 15: Average (blue) and maximum (red) contrast as a function of time for 4QPM 1550 for different latency prescriptions. Note that the scale is logarithmic. The effect of latency is seen here for the case with no offset between the target and the reference as well as no noise. In this case the contrast is entirely limited by the latency effects (without closing CCC).

Results for noiseless simulations at 15.50 μm with folding times of 3000 and 10,000 seconds are shown in top panels of Figure 16 (left and right respectively). As expected, longer folding times lead to longer integration times in order to achieve the same level of image quality. We observe a similar behavior when increasing the latents initial value (bottom left panel; 10% of previous image with a folding time of 3000 seconds). In any case, Figure 17 shows that the addition of an offset or noise completely dominates the small signal from the latents observed. Our simulations therefore suggest that because mainly of background noise, latents can be mitigated even when the CCC mechanism is not used, within our model for latency.

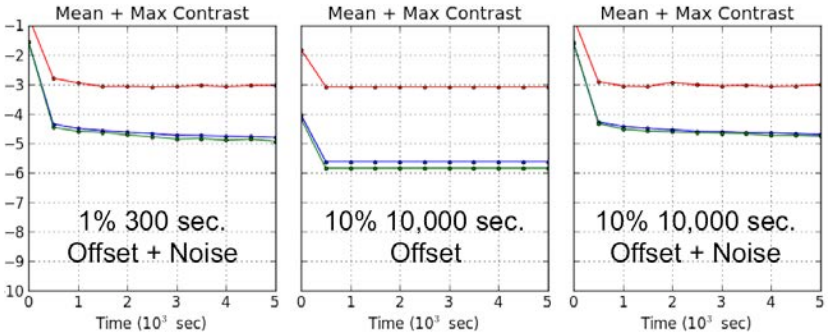

Figure 16: The effect of latency, with various prescriptions, is dominated by target/reference offset and background noise. This is only one pair of target and reference and the offset is 10 mas.

5 Summary & Concluding Remarks

We presented the results of simulations in which we manipulate multiple coronagraphic images to mimic latency effects during TA and estimate effects on the quality of final

coronagraphic science images. The goal of this study is (1) to assess whether the use of the Contamination Control Cover (CCC) is necessary during TA and if latents can be mitigated and (2) to derive raw contrast curves to assess the 4QPM performances. The adopted behavior for latency is an exponential decay starting at 1% of the previous image and decaying over 300 seconds (factor 1/e), and these factors are applied every time the detector is reset, which in coronagraphy, is every 0.242 seconds. We model a Vega-like spectrum with a target star of magnitude 6 and a reference star of magnitude 4 and simulate an exposure time of 10,000 seconds. We include various sources of noise such as stellar photon, detector, and background photon noise and show that latents are quickly overwhelmed by the total noise at all wavelengths. The relative contribution of the background noise at 15.50 μm also further limits the raw contrast performance of the 4QPM 1550. At shorter wavelengths, the background noise is less important and the main limiting factor is the slew accuracy, which introduces offsets between the target and reference stars. Our simulations assume a range of slew accuracy, based on a range of possibilities known from the ACS CDA. The accuracy of these small angle maneuvers (SAMs) will be revised in late 2013 based on updates to the Line Of Sight (LOS) system.

In general, our simulations suggest that raw contrast of ~$10^{-5.5}$-$10^{-4.5}$ can be achieved with MIRI 4QPM coronagraphs. We emphasize once more that raw contrast is defined as the azimuthal average of the contrast image normalized by the peak of an off-axis PSF, and that it does not constitute a detection limit but is rather only a useful metric to assess the performances of the 4QPM. We also investigated various latency prescriptions and concluded that the background noise and target/reference offsets still dominate over latency. Our results suggest that the use of the CCC during target acquisition is not vital and that latents do not impact science images for integration longer than ~500-1000 seconds. These conclusions should only hold true for the stellar spectral type and magnitudes used here however. We therefore warn the reader that performances of the coronagraphs derived in this report represent conservative limits, considering in particular the fact that latency might behave differently than the prescription used in our simulations. Further detector testing planning at JPL and ISIM level should emphasize the need for a better characterization of latent images on the MIRI detectors.

Finally, we point out, as suggested by Greene & Walker (2013), that using the detector FLUSH mode appears to further reduce the initial strength of latents by a factor of ~7. In the advent of latents behaving significantly differently from what assumed here, the use of the FLUSH mode during rotation of the filter wheel should be considered in order to limit the impact of latents on the final image. The possibility of performing a detector ANNEAL is also being considered in order to mitigate hard latent images.

6 References

Glasse, A.C.H. et al. 2010, *The Throughput and Sensitivity of the JWST Mid-Infrared Instrument*. SPIE Proceedings Vol. 7731, Space Telescopes and Instrumentation 2010: Optical, Infrared, and Millimeter Wave

Greene, T. & Walker, H. 2013, *Detector Latent Decay FM IMG-RAD-12/FM MRS-RAD-12*. MIRI FM Performance Test Report MIRI-TR-00002-ARC

Hines, D.C., Lajoie, C-P, & Soummer, R. 2014, JWST-STScI Technical Reports, in preparation.

Lajoie, C-P, Soummer, R., & Hines D. 2013, *Simulations of Target Acquisition with MIRI Four-Quadrant Phase Mask Coronagraph (II)*. STScI JWST Technical Reports

JWST-STScI-003065

Renouf, I. et al. 2011, *JWST Mid-Infrared Instrument OBA Design Description*. MIRI-DD-00001-AEU

Soummer, R. & Makidon, R. 2010, *Simulations of MIRI Coronagraphic Images*. STScI JWST Technical Reports JWST-STScI-001952